

EmCa - Electromagnetic-Cascades Simulation Package

S. Meighen-Berger^{a,*}, A. Fedynitch^b, M. Huber^a

^aTechnical University of Munich, Arcisstr. 21, D-80333 Munich

^bUniversity of Alberta, 116 St & 85 Ave, Edmonton, AB T6G 2R3, Canada

Abstract

Electromagnetic-Cascades (EmCa) is a Python package for the simulation of electromagnetic cascades in various materials. The showers are modeled using cascade equations and the relevant interactions, specifically pair production, Bremsstrahlung, Compton scattering and ionization. This methodology has the advantage of being computationally inexpensive and fast, unlike Monte Carlo methods. The code includes low and high energy material effects, allowing for a high range of validity of the simulation results. EmCa is easily extendable and offers a framework for testing different electromagnetic interaction models. In combination with MCEq, a Python package for hadronic particle showers using cascade equations, full simulations of atmospheric fluxes can be done.

Keywords: Electromagnetic Cascades, Cascade Equations, Atmospheric Showers

1. Introduction

Due to the increasing interest in multi-messenger astronomy, there is an ever growing need of high precision atmospheric particle flux calculations [1].
 Measurements of the neutrino mass hierarchy [2], neutrino oscillations [3], and the cosmic ray primary flux [4] rely on precise knowledge of atmospheric neutrino and muon fluxes. On the other hand, when studying astrophysical particles, the atmospheric particle flux is a background signal which needs to be modelled. There are different approaches to simulating such particle cascades. One is the use of Monte Carlo methods to simulate on an event by event basis, as used in CORSIKA [5]

or EGS5 [6]. While Monte Carlo methods have proven successful, they come with a high computational cost. If an average particle flux at high energies (above 1 GeV) is of interest, an iterative approach using cascade equations offers a similar precision to Monte Carlo calculations without the computational expense [7, 8]. This allows for rapid testing and scanning of different models and their parameters. Cascade equation approaches are implemented, for example, in MCEq [9] and CONEX [10]. EmCa¹ uses similar numerical methods employed in MCEq for the calculation of particle cascades and provides an electromagnetic model, allowing for the simulation of electromagnetic showers. As a framework, it is designed to be easily

*Corresponding author

30 extendable, allowing a user to include their own
 interaction models, density models, and materials.
 Additionally, since the calculations are computa-
 tionally inexpensive, testing and prototyping can be
 done at a much faster pace than with Monte Carlo
 35 methods. Note that unlike the direct approach used
 here, it is possible to write an adjoint cascade the-
 ory as described in [11].

This paper introduces the EmCa framework, start-
 ing with a description of the cascade equations, fol-
 40 lowed by the used electromagnetic model. We de-
 signed the interaction model to be valid for a broad
 range of elements and many orders of magnitude
 in energy, starting at 10 MeV up to energies where
 photo-hadron interactions become relevant. After-
 45 wards, in section (4) the numerical implementation
 is discussed. Finally results using EmCa are com-
 pared with Monte Carlo simulations in section (5).

2. Coupled Cascade Equations

Instead of simulating single particles, the average
 particle flux Φ , which is defined to be

$$\Phi = \frac{dN}{dAd\Omega dt} [\text{cm}^{-2}\text{sr}^{-1}\text{s}^{-1}], \quad (1)$$

is calculated using cascade equations. For convenience we define the slant depth variable X , which describes the geometric trajectory through a material, as

$$X(h_0) = \int_0^{h_0} dl \rho(l), \quad (2)$$

where h_0 is the current position and ρ the density of the material. Using the slant depth, the transport

equations for an electromagnetic particle i are

$$\begin{aligned} \frac{d\Phi_i(E, X)}{X} = & -\frac{\Phi_i(E, X)}{\lambda_i(E)} \\ & -\frac{\partial}{\partial E} (\mu(E)\Phi_i(E, X)) \\ & + \sum_l \int_E^\infty dE_l \frac{1}{\sigma(E_l)} \\ & \times \left(\frac{d\sigma_{l(E_l) \rightarrow i(E)}}{dE} \frac{\Phi_l(E_l, X)}{\lambda_l(E_l)} \right). \end{aligned} \quad (3)$$

In the above equation, E is the energy of the parti-
 50 cle flux, σ the cross section, λ the interaction length
 and μ a loss parameter. The first two terms de-
 scribe losses due to interactions and ionization re-
 spectively. The last one is a source term containing
 55 the production of particle i by particle l where the
 sum runs over all particles.

In the case of EmCa the considered particles are γ ,
 e^\pm , and μ^\pm . Muons were added to the cascade to
 allow the electromagnetic cascade to couple back to
 hadronic showers.

60 For the simulation the density of the background
 medium is required at each step. This requires a
 depth-dependent model of air. In the following sim-
 ulations we chose to use the U.S. Standard Atmo-
 sphere [12].

3. Model

The electromagnetic model implemented in
 EmCa contains four types of interactions, namely
 pair production, Bremsstrahlung, Compton scat-
 tering, and ionization. The differential cross sec-
 tions used for pair production and Bremsstrahlung
 were taken from [13]. Other calculations of these
 interactions are Bethe and Heitler's [14], which is
 the foundation of the modern understanding of pair

production, or Migdal's derivations [15], which includes the LPM effect. More recent calculations allow the treatment of targets of finite thickness done for example by Zakharov [16] and Baier and Katkov [17, 18]. Klein's comparison of pair production in different regimens [19] offers an overview of these calculations.

The advantage of the cross sections by Tsai, is that they do not possess an explicit density dependence and therefore allow the numerical treatment described in section (4). Density effects, such as Landau-Pomeranchuk-Migdal (LPM) [20, 21] and dielectric [22, 23] effects, are treated separately, as described in Section (3.1).

For pair production, $d\sigma/dE$ has the form

$$\frac{k}{\alpha r_0^2} \frac{d\sigma}{dE} = \left[\frac{4}{3}x^2 - \frac{4}{3}x + 1 \right] \times \left[Z^2 \left(\phi_1 - \frac{4}{3} \log Z - 4f \right) + Z \left(\psi_1 - \frac{8}{3} \log Z \right) \right] - \frac{2}{3}x \left[Z^2 (\phi_1 - \phi_2) + Z(\psi_1 - \psi_2) \right] \quad (4)$$

and for Bremsstrahlung

$$\frac{k}{\alpha r_0^2} \frac{d\sigma}{dk} = \left[y^2 - \frac{4}{3}y + \frac{4}{3} \right] \times \left[Z^2 \left(\phi_1 - \frac{4}{3} \log Z - 4f \right) + Z \left(\psi_1 - \frac{8}{3} \log Z \right) \right] - \frac{2}{3}(1-y) \times \left[Z^2 (\phi_1 - \phi_2) + Z(\psi_1 - \psi_2) \right]. \quad (5)$$

In Equations (4) and (5), ϕ_i and ψ_i describe screening effects, Z is the atomic number of the background medium, f a Coulomb correction, α the fine structure constant and r_0 the classical electron radius. For convenience we introduce $x = E/k$ and

$y = k/E$, with E being the electron energy and k the photon energy. To calculate the screening functions, we use a Thomas-Fermi-Molier model, as described in [13]. Figure (1) shows a plot of the differential cross sections for the different processes for a primary energy of 1 PeV.

The corresponding integrated cross sections are shown in Figure (2), where the channel $e \rightarrow e$ was dropped since the integrated cross section is the same as $e \rightarrow \gamma$. From these the interaction lengths, λ , are calculated using

$$\lambda = \frac{A}{N_A} \frac{1}{\sigma}, \quad (6)$$

where N_A is the Avogadro number and A the atomic mass of the background medium. Muon pair

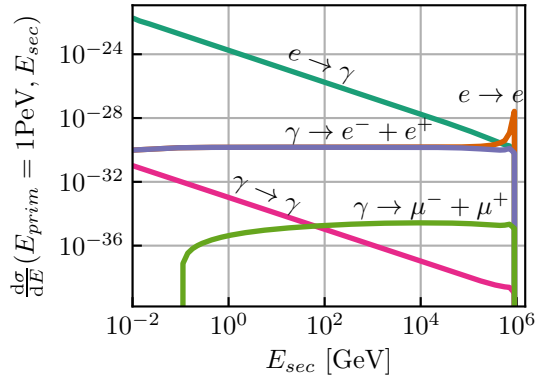


Figure 1: The differential cross sections for the interactions implemented in EmCa. The processes are Bremsstrahlung (teal and orange), pair production (blue and green) and Compton scattering (purple).

production due its natural low energy cutoff can be treated in a simpler fashion, since screening is irrelevant. For this reason, a different cross section, described in [24], is implemented. The form of the differential cross section is

$$\frac{d\sigma_\mu}{dE} = \frac{4\alpha r_e^2 Z^2}{k} \left(1 - \frac{4}{3}(x - x^2) \right) \log(W). \quad (7)$$

Where $x = E_\mu/k$ and the weight factor W is defined as

$$W = \frac{BZ^{-1/3}}{D} \frac{m_\mu}{m_e} \frac{1+(D\sqrt{e}-2)\frac{\delta}{m_\mu}}{1+BZ^{-1/3}\sqrt{e}\frac{\delta}{m_e}}. \quad (8)$$

In turn the parameters are $B = 202.4$ and $D = 1.49$ for hydrogen and $B = 183$ and $D = 1.54A^{0.27}$ otherwise. Finally $\delta = \frac{m_\mu^2}{2k(x-x^2)}$ and $\sqrt{e} = 1.6487$. Note that as expected, the shape of the differential cross sections for muon and electron pair production are similar. An added benefit of this definition of the cross section is that it is implemented in CORSIKA as well, allowing for a direct comparison.

Compton scattering needs to be added for secondary spectra with a low energy cutoff below 100 MeV, when this channel becomes relevant compared to pair production. Figure (2), shows the total cross sections for the implemented processes. At low energies the total cross section for Compton scattering dominates over those from pair production. For Compton scattering the Klein-Nishina cross section [25] is used, which is a generalized version of Compton- and Thomson-scattering. It has the form

$$\frac{d\sigma}{dk} = \frac{\pi r_0^2}{m_e} \frac{Z}{\kappa^2} \left(\epsilon + \frac{1}{\epsilon} - \frac{2}{\kappa} \frac{1-\epsilon}{\epsilon} + \frac{1}{\kappa^2} \left[\frac{1-\epsilon}{\epsilon} \right]^2 \right), \quad (9)$$

with $\epsilon = k/k_0$, $\kappa = k_0/m_e$, where $k_0 = E_{\text{prim}}/m_e$ and $k = k_{\text{sec}}/m_e$. Due to the nature of two body scattering processes when integrating over Equation (9) a minimal energy needs to be introduced

$$k_{\text{min}} = k_0/(2\kappa + 1).$$

For the description of ionization losses we use the energy loss tables generated by ESTAR [26], which describe μ in Equation (3). The collision stopping powers in those tables are calculated using [27, 28].

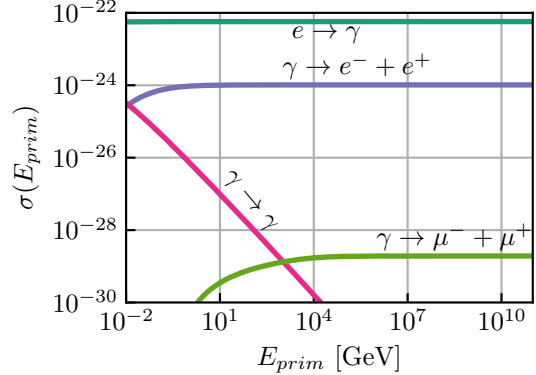


Figure 2: The integrated cross section for the different production channels. Other interactions only play a subleading role in the energy ranges of interest and can be ignored.

3.1. Material Effects

To allow for a higher range of validity in energy we account for additional material effects, i.e. dielectric suppression [22, 23] and the LPM effect [15, 21].

The dielectric effect is treated as a suppression factor, $S_{\text{die}}(k)$, of the differential cross section of the form

$$S_{\text{die}}(k) = \frac{k^2}{k^2 + (\gamma \cdot \hbar \omega_p)^2}, \quad (10)$$

where ω_p is the plasma frequency of the material. Due to the density dependence of $\omega_p \propto \sqrt{\rho}$ the differential cross sections become density dependent. The point at which the dielectric effect becomes relevant can be estimated by calculating the ratio $r = \omega_p/m_e$. For air at standard density $\omega_p(\text{Air}) = 6.6 \times 10^{-10}$ GeV and $r \approx 10^{-6}$, which leads to the differential cross section starting to be suppressed at about $E_{\text{sec}} = E_{\text{prim}} \times 10^{-6}$. In atmospheric showers this does reduce the production of low energy photons at the start of the shower. Later in the shower development, where far more low energy photons are produced, the difference be-

90 comes negligible. We show this effect in Figure (3),
 where we used an air column with constant density
 $\rho = 0.00123 \text{ g/cm}^3$. This leads to a conservative
 estimate of the dielectric suppression.

95 In most cases the dielectric effect can safely be ig-
 nored in air. Note, that due to the inclusion of the
 dielectric effect the cross section for Bremsstrahlung
 no longer diverges for $k \rightarrow 0$, allowing for precise
 calculations of the total cross section. Thus, even
 100 for air showers, where there is no direct physical
 effect, the dielectric effect allows for the calculation
 of the total cross section, without the introduction
 of an unphysical low energy cutoff.

105 On the other hand for materials with a larger Z ,
 metals for example, typical values of $r \approx 10^{-4}$ re-
 sult in a larger relevance of the dielectric effect.

The LPM effect suppresses the interaction cross
 sections at high energies. This can be accounted for
 by adding a suppression term [21] of the form

$$S_{\text{LPM}} = \sqrt{\frac{kE_{\text{LPM}}}{E(E-k)}}, \quad (11)$$

with

$$E_{\text{LPM}} = \frac{7.7 \text{ TeV} X_0}{\rho}, \quad (12)$$

to the differential cross section. This again would
 introduce a density dependence to the cross section.
 Due to the employed numerical methods, discussed
 in section (4), we wish to avoid this and instead
 treat the LPM effect by rescaling the interaction
 lengths λ_{Pre} , defined in Equation (6), according to

$$\lambda_{\text{True}} = \left(\frac{E_{\text{prim}}}{E_{\text{LPM}}} \right)^{1/2} \lambda_{\text{Pre}}, \text{ for } E_{\text{LPM}} < E_{\text{prim}}. \quad (13)$$

This allows the shape of the differential cross section
 to remain density independent, and the interaction length
 only needs to be re-scaled according to the current density. In Figure (3), we show the

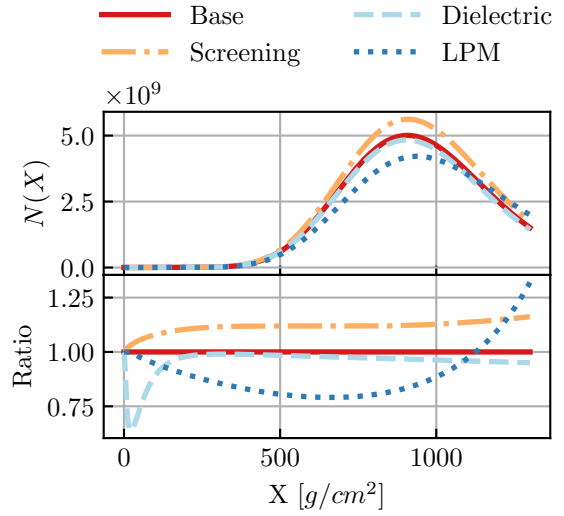


Figure 3: The particle number changes to an atmospheric shower due to different material effects and screening. Plotted is the total number of particles in a 10 EeV γ primary initiated shower in air. The low energy cutoff was chose to be 86 MeV. Accounting for the dielectric suppression only leads to minor changes in the shower development, unlike screening and the LPM effect.

110 consequences of including the LPM effect (pink) for
 air showers when compared to the baseline theory
 (green) without it. Figure (4) shows the change
 in the energy balance of a shower initiated by a
 115 10 EeV photon in air, for the different material ef-
 fects. The total energy (line), the energy carried
 by photons (dashed) and the total energy carried
 by electrons (dotted) is plotted and compared to
 the baseline theory. All these effects change the
 amount of energy carried by electrons, which is rel-
 evant to fluorescence experiments such as at Auger
 120 [29] and TA [30]. Fluorescence is generated by col-
 lision losses of charged particles in the atmosphere.
 By including these effects, the energy in the electron
 part of the shower is reduced, reducing fluorescence.

¹²⁵ Not including these effects would lead to an over-estimation of the deposited energy of atmospheric cascades.

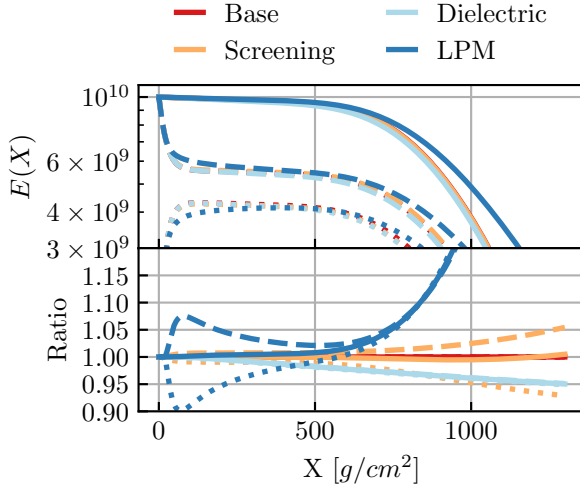


Figure 4: The change of the energy balance of a shower initiated by 10 EeV Photon in air. The total energy (line), the energy carried by photons (dashed) and the energy carried by electrons (dotted) is shown.

4. Numerical Form

Similar to MCEq, the cascade equations are discretized on a logarithmic grid with ten grid points per energy logarithmic energy decade. The particle fluxes are arranged in a state vector $\vec{\Phi}$ of the form

$$\vec{\Phi} = \left(\vec{\Phi}^{e^-}, \vec{\Phi}^{e^+}, \vec{\Phi}^\gamma, \vec{\Phi}^{\mu^-}, \vec{\Phi}^{\mu^+} \right)^T \quad (14)$$

with sub-vectors of the form

$$\vec{\Phi}^i = \left(\Phi_{E_0}^i, \Phi_{E_1}^i, \dots, \Phi_{E_N}^i \right)^T. \quad (15)$$

The differential, $\frac{d\sigma_{li}}{dE}$ and total cross sections, σ_l , are arranged in a matrix \mathbf{C}_{li} with elements

$$c_{l(E_l)i(E_i)} = \Delta E_l \frac{1}{\sigma(E_l)} \left\langle \frac{d\sigma_{l(E_l) \rightarrow i(E_i)}}{dE_i} \right\rangle \quad (16)$$

and shape

$$\mathbf{C}_{li} = \begin{pmatrix} c_{l(E_0)i(E_0)} & \dots & c_{l(E_1)i(E_0)} \\ 0 & \dots & c_{l(E_1)i(E_N)} \\ \dots & \dots & \dots \\ 0 & \dots & c_{l(E_N)i(E_N)} \end{pmatrix}. \quad (17)$$

Note that due to energy conservation \mathbf{C}_{li} is an upper triangular matrix. In the above calculations bin averaged differential cross sections defined in equations (18, 19).

Due to the nature of electromagnetic cascades evolving very quickly and having only a limited amount of possible interactions, numerical errors as small as 0.1% affect the shower development. As a cross-check, the calculation of σ and $\frac{d\sigma}{dE}$, from Equation 3, are kept separate. Integrations of the differential cross sections are performed in fractional energy space by substituting the secondary's energy E_{sec} , with $x = \frac{E_{\text{sec}}}{E_{\text{prim}}}$. Figure (5) shows the differential cross section for $e \rightarrow e$ in fractional energy space. Integrations are then performed on

$\frac{1}{E_{\text{prim}}} \frac{d\sigma}{dx}(x, E_{\text{prim}})$. In this scheme $\sigma(E)$ is calculated by integrating from 0 to 1.

We average $\frac{d\sigma}{dE}$ and its first and second moments for each energy bin. This means for each energy bin three integrals are performed,

$$\begin{aligned} \mu_{l,i}^0 &= \left\langle \frac{d\sigma}{dE_i} (E_l, E_i) \right\rangle_{l,i} = \int \frac{d\sigma}{dE_i} (E_l, E_i) dE_i \\ \mu_{l,i}^1 &= \left\langle \frac{d\sigma}{dE_i} (E_l, E_i) \right\rangle_{l,i}^{\text{Mom 1}} = \int E_i \frac{d\sigma}{dE_i} (E_l, E_i) dE_i \\ \mu_{l,i}^2 &= \left\langle \frac{d\sigma}{dE_i} (E_l, E_i) \right\rangle_{l,i}^{\text{Mom 2}} = \int E_i^2 \frac{d\sigma}{dE_i} (E_l, E_i) dE_i. \end{aligned} \quad (18)$$

The integrals are calculated over the bin widths using a Tanh-Sinh quadrature, and defining the maximum of the function as an integration node. Then for each bin, defined by the center E_i and the width

ΔE_i , the equation

$$\begin{bmatrix} \Delta E_{i-1} & \Delta E_i & \Delta E_{i+1} \\ E_{i-1}\Delta E_{i-1} & E_i\Delta E_i & E_{i+1}\Delta E_{i+1} \\ E_{i-1}^2\Delta E_{i-1} & E_i^2\Delta E_i & E_{i+1}^2\Delta E_{i+1} \end{bmatrix} \times \begin{bmatrix} x_1 \\ x_2 \\ x_3 \end{bmatrix} = \begin{bmatrix} \mu_{l,i}^0 \\ \mu_{l,i}^1 \\ \mu_{l,i}^2 \end{bmatrix}, \quad (19)$$

is solved. This methodology has the advantage of conserving energy and particle number.

In Figure (5), the binned differential cross section (EmCa) is compared to the analytic one. The vertical lines show the position of the average of each version, which shows a very high agreement. The functions are plotted against the fractional energy carried by the secondary particle $x = E_{\text{sec}}/E_{\text{prim}}$. The interaction matrices from Equation (17) are

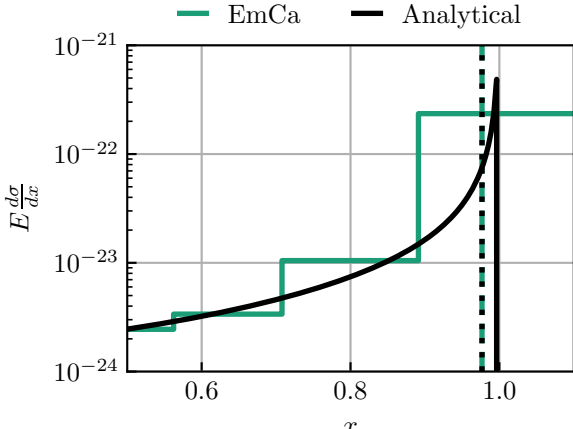


Figure 5: Binned (EmCa) version of the differential cross section for $e \rightarrow e$ and its analytical form. The functions are plotted against the fractional energy $x = E_{\text{sec}}/E_{\text{prim}}$ of the secondary particle. The dashed vertical lines are the position of the average of the binned and analytic versions. The high agreement is achieved by including first and second moments in the calculations.

then grouped together in a single matrix \mathbf{C} of the form

$$\mathbf{C} = \begin{pmatrix} \mathbf{C}_{e^-e^-} & \dots & \mathbf{C}_{\mu^+e^-} \\ \mathbf{C}_{e^-e^+} & \dots & \mathbf{C}_{\mu^+e^+} \\ \dots & \dots & \dots \\ \mathbf{C}_{e^-\mu^+} & \dots & \mathbf{C}_{\mu^+\mu^+} \end{pmatrix}. \quad (20)$$

The interaction lengths are organized into a diagonal matrix $\mathbf{\Lambda}_{\text{int}}$ of the form

$$\mathbf{\Lambda}_{\text{int}} = \text{diag}\left(\frac{1}{\lambda_{\text{int}}^{e^-}(E_0)}, \dots, \frac{1}{\lambda_{\text{int}}^{e^-}(E_N)}, \frac{1}{\lambda_{\text{int}}^{e^+}(E_0)}, \dots, \frac{1}{\lambda_{\text{int}}^{e^+}(E_N)}, \dots\right). \quad (21)$$

Finally, the ionization loss term is treated by discretizing the loss parameter μ in energy and approximating the differential using a seven-point stencil method. These steps are discussed more in-depth in section (4.1). The resulting operator is written as \mathbf{L} . Approximating Equation (3) using the above definitions results in

$$\frac{d\vec{\Phi}}{dX} = (-\mathbf{L} + (-1 + \mathbf{C})\mathbf{\Lambda}_{\text{int}})\vec{\Phi}. \quad (22)$$

Combining the terms, besides $\vec{\Phi}$, results in a single derivative operator. Figure (6) shows the non-zero elements of this resulting operator. To solve Equation (22) we use an explicit Euler solver. An integration step has the form

$$\vec{\Phi}(X + \Delta X) = (-\mathbf{L} + (-1 + \mathbf{C})\mathbf{\Lambda}_{\text{int}}) \times \vec{\Phi}(X) \Delta X. \quad (23)$$

4.1. Ionization

Ionization losses are treated as a continuous loss term in the cascade equation. This turns the ordinary differential equation into a partial one. Implies the need for an implicit solver method. To

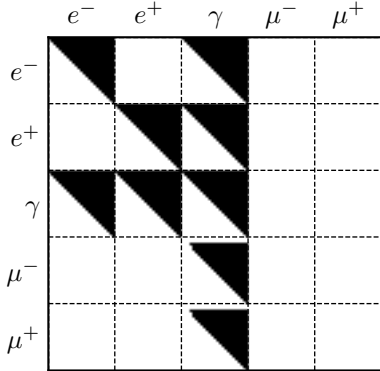


Figure 6: The non-zero values of the equation matrix. Each non-zero block corresponds to a specific interaction, e.g. the first block (e^-, e^-) describes the electron self-interaction.

avoid this, the continuous loss terms are discretized using a seven-point stencil method. In this approximation, a derivative of a function $f(x)$ is written as

$$\begin{aligned} \frac{\partial f}{\partial x} \approx \frac{1}{60h} & (-1f(x-3h) + 9f(x-2h) \\ & - 45f(x-h) + 0f(x+0h) \\ & + 45f(x+h) - 9f(x+2h) \\ & + 1f(x+3h)), \end{aligned} \quad (24)$$

where h is the used step size. The differential operator, $\hat{\mathbf{L}}$ is then calculated by multiplying the approximation for ∂_E on the left with $\frac{1}{E}$ and from the right with $\mu(E)$. Applying this definition to the ionization losses, the discretized form can be written as

$$\partial_E \mu(E) \Phi = \hat{\mathbf{L}} \Phi. \quad (25)$$

The $1/E$ term appears due to the use of a logarithmic grid, and $\hat{\mathbf{L}}$ is calculated using the above mentioned stencil method. A comparison between the ESTAR tables (red), the binned version in EmCa (blue) and an energy loss simulation using EmCa (green) is shown in Figure (7). The resulting energy

losses from the simulation show a high agreement, $\approx 3\%$, with the ESTAR table results. In EmCa

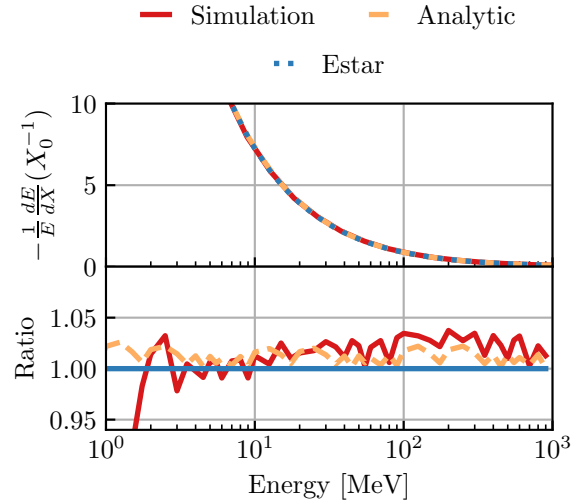


Figure 7: The ionization loss function implemented in EmCa. The tables from ESTAR (red), the binned version in EmCa (blue) and energy loss simulation results (green) are compared. To simulate the average energy losses, electrons with different energies are injected into the material and propagated through it, while all radiative losses are switched off. Using the average energy loss per integration step we normalize it to X_0 . The 'spikes' in the ratio plot are due to the discretization employed in EmCa.

the recommended low energy cutoff is defined by E_{crit} using Rossi's definition [31]. E_{crit} is the point at which collision losses start to dominate the electron energy losses over radiative ones. The critical energy is defined as

$$E_{\text{crit}}^{\text{gas}} = \frac{710 \text{ MeV}}{Z+0.92}, \quad (26)$$

and

$$E_{\text{crit}}^{\text{solid}} = \frac{610 \text{ MeV}}{Z+1.24}. \quad (27)$$

For air the critical energy is 86 MeV.

5. Comparisons

In the following we compare results using EmCa, including all previously mentioned effects, to CORSIKA air shower simulations for highly energetic particles and EGS4 [32] for low energetic ones.

5.1. CORSIKA

We show a comparison between particle numbers taken from [10] and EmCa for two different low energy cuts in Figure (8). On the left, the cut was set to 1 MeV and on the right to 1 GeV. EmCa shows a high agreement with the CORSIKA results in both cases. In the 1 MeV cutoff case, there is a discrepancy between the CONEX (CE) / Hybrid results and the CORSIKA (MC) / EmCa ones. In [10] this was attributed to three-dimensional effects and corrected with a scaling factor. Due to the agreement between EmCa and the CORSIKA results, without the need for such a scaling, we believe the differences are not due to any additional effects.

Additionally we compared the average development of the shower maximum, X_{\max} , of photon initiated showers. In Figure (9) a comparison between EmCa and the results shown in [33], where CORSIKA (MC) was used, is shown. The drop off in agreement at higher energies is a result of the approximation used in EmCa to treat the LPM effect, defined in Equation (13). The theory line is calculated using the Heitler Model [34], in which the shower maximum is approximated by

$$X_{\max} = X_0 \ln \left(\frac{E_{\text{prim}}}{E_{\text{crit}}} \right), \quad (28)$$

where for all calculations $E_{\text{crit}} = 86$ MeV. In the theoretical model the LPM effect is not accounted

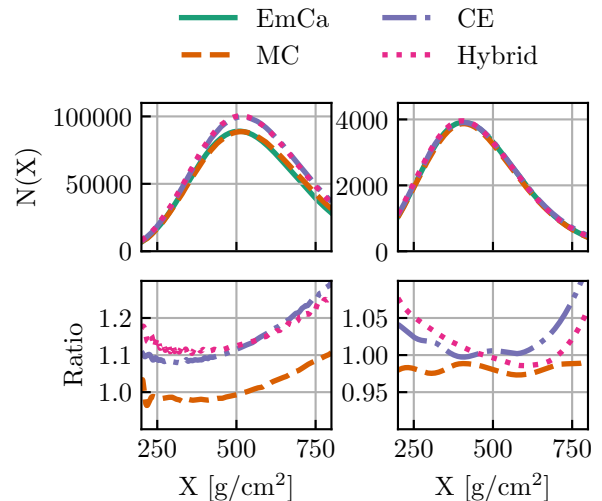


Figure 8: Comparison between the $e^- + e^+$ results from [10] and EmCa with a primary photon of 100 TeV. Left particles above 1 MeV were tracked and on the right particles above 1 GeV. Results using different methods were plotted: Monte Carlo (CORSIKA, yellow), cascade-equations (CONEX, blue), hybrid (CORSIKA + CONEX, pink) and EmCa (green). The deviations are calculated as a ratio to EmCa.

for, which explains the discrepancy at high energies.

5.2. EGS4

In Figure (10) we compare particle number calculations of EmCa and EGS4, in iron. The low energy cutoff was set to 1.5 MeV. In the simulation an electron with 30 GeV was injected into a uniform block of iron. The deviations are due to different definitions of the cross sections, the dielectric effect and the additional interactions included in EGS4. It is designed for energy ranges between 1 MeV and 100 GeV, which holds true for the newer version EGS5, and includes low energy interactions such as Moller Scattering, Bhabha scattering, multiple scattering

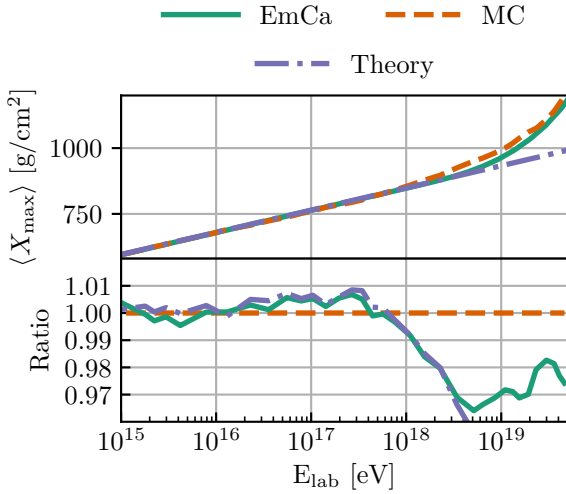


Figure 9: The development of X_{\max} for photon initiated showers dependent on energy are shown. The results using EmCa are compared to those from [33] using CORSIKA (MC). Ratios are shown in the bottom plot.

and the photoelectric effect, which are not included in EmCa.

155 6. Conclusion

EmCa provides a fast and precise framework and model for the calculation of electromagnetic cascades in different materials. By achieving a similar precision to Monte Carlo based programs and 160 through its modular structure, EmCa is a useful testing ground for new interaction models. In [36], different suppression mechanisms and their effect on extremely high energy air showers were discussed. Using EmCa we were able to do a similar study quickly, as seen in Figure (3). Additionally, combined with the implemented model, it can be used as a fast method to estimate atmospheric backgrounds for a wide array of experiments, espe- 165 180

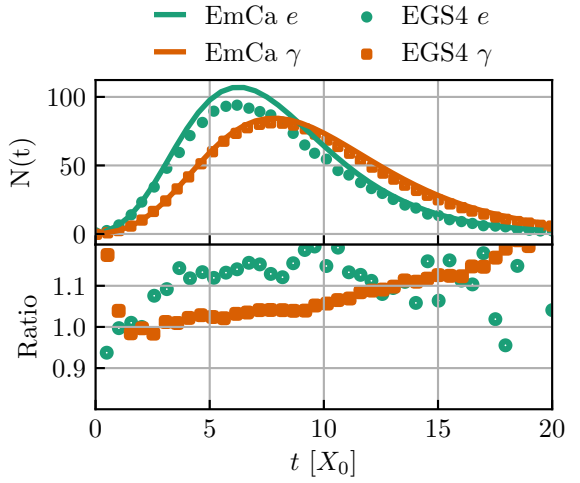


Figure 10: Comparison between the EGS4 and EmCa results of a electron initiated 30 GeV shower. Data for the EGS4 results are taken from [35]. The particle numbers between the simulations show a high agreement, with the deviation between the two being under 10% for most of the shower. The x-Axis is plotted in units of radiation length.

cially in combination with MCEq. The next steps 170 will be to implement full three-dimensional calculations and additional cross sections.

Acknowledgements

The material presented in this publication is based upon work supported by the Sonderforschungsbereich Neutrinos and Dark Matter in 175 Astro- and Particle Physics (SFB1258).

References

[1] M. Ahlers, F. Halzen, IceCube: Neutrinos and multi-messenger astronomy, *PTEP* 2017 (12) (2017) 12A105. doi:10.1093/ptep/ptx021.

[2] W.-l. Guo, Atmospheric neutrinos in JUNO, *J. Phys. Conf. Ser.* 888 (1) (2017) 012205. [doi:10.1088/1742-6596/888/1/012205](https://doi.org/10.1088/1742-6596/888/1/012205).

[3] M. G. Aartsen, et al., Measurement of Atmospheric Neutrino Oscillations at 6–56 GeV with IceCube Deep-Core, *Phys. Rev. Lett.* 120 (7) (2018) 071801. [arXiv:1707.07081](https://arxiv.org/abs/1707.07081), [doi:10.1103/PhysRevLett.120.071801](https://doi.org/10.1103/PhysRevLett.120.071801).

[4] M. G. Aartsen, et al., Characterization of the Atmospheric Muon Flux in IceCube, *Astropart. Phys.* 78 (2016) 1–27. [arXiv:1506.07981](https://arxiv.org/abs/1506.07981), [doi:10.1016/j.astropartphys.2016.01.006](https://doi.org/10.1016/j.astropartphys.2016.01.006).

[5] D. Heck, J. Knapp, J. N. Capdevielle, G. Schatz, T. Thouw, CORSIKA: A Monte Carlo code to simulate extensive air showers.

[6] H. Hirayama, Y. Namito, A. F. Bielajew, S. J. Wilderman, W. R. Nelson, The EGS5 code system.

[7] T. K. Gaisser, Cosmic rays and particle physics, Cambridge, UK: Univ. Pr. (1990) 279 p, 1990.

URL <http://www.cambridge.org/uk/catalogue/catalogue.asp?isbn=0521326672>

[8] P. Lipari, Lepton spectra in the earth's atmosphere, *Astropart. Phys.* 1 (1993) 195–227. [doi:10.1016/0927-6505\(93\)90022-6](https://doi.org/10.1016/0927-6505(93)90022-6).

[9] A. Fedynitch, R. Engel, T. K. Gaisser, F. Riehn, T. Stanev, Calculation of conventional and prompt lepton fluxes at very high energy, *EPJ Web Conf.* 99 (2015) 08001. [arXiv:1503.00544](https://arxiv.org/abs/1503.00544), [doi:10.1051/epjconf/20159908001](https://doi.org/10.1051/epjconf/20159908001).

[10] T. Bergmann, R. Engel, D. Heck, N. N. Kalmykov, S. Ostapchenko, T. Pierog, T. Thouw, K. Werner, One-dimensional Hybrid Approach to Extensive Air Shower Simulation, *Astropart. Phys.* 26 (2007) 420–432. [arXiv:astro-ph/0606564](https://arxiv.org/abs/astro-ph/0606564), [doi:10.1016/j.astropartphys.2006.08.005](https://doi.org/10.1016/j.astropartphys.2006.08.005).

[11] A. A. Lagutin, V. V. Uchaikin, Adjoint cascade theory in astroparticle physics, *Izv. Altais. Gos. Univ.* 9 (1998) 4–32.

[12] NASA, U.S. Standard Atmosphere, 1976, Washington D.C., 1976, NASA-TM-X-74335.

[13] Y.-S. Tsai, Pair Production and Bremsstrahlung of Charged Leptons, *Rev. Mod. Phys.* 46 (1974) 815, [Erratum: *Rev. Mod. Phys.* 49, 521 (1977)]. [doi:10.1103/RevModPhys.46.815](https://doi.org/10.1103/RevModPhys.46.815), [10.1103/RevModPhys.49.421](https://doi.org/10.1103/RevModPhys.49.421).

[14] H. Bethe, W. Heitler, On the Stopping of fast particles and on the creation of positive electrons, *Proc. Roy. Soc. Lond.* A146 (1934) 83–112. [doi:10.1098/rspa.1934.0140](https://doi.org/10.1098/rspa.1934.0140).

[15] A. B. Migdal, Bremsstrahlung and pair production in condensed media at high energies, *Phys. Rev.* 103 (1956) 1811–1820. [doi:10.1103/PhysRev.103.1811](https://doi.org/10.1103/PhysRev.103.1811). URL <https://link.aps.org/doi/10.1103/PhysRev.103.1811>

[16] B. G. Zakharov, Landau-Pomeranchuk-Migdal effect for finite size targets, *Pisma Zh. Eksp. Teor. Fiz.* 64 (1996) 737, [JETP Lett. 64, 781 (1996)]. [arXiv:hep-ph/9612431](https://arxiv.org/abs/hep-ph/9612431), [doi:10.1134/1.567248](https://doi.org/10.1134/1.567248).

[17] V. N. Baier, V. M. Katkov, Theory of the landau-pomeranchuk-migdal effect, *Phys. Rev. D* 57 (1998) 3146–3162. [doi:10.1103/PhysRevD.57.3146](https://doi.org/10.1103/PhysRevD.57.3146). URL <https://link.aps.org/doi/10.1103/PhysRevD.57.3146>

[18] V. N. Baier, V. M. Katkov, Influence of a medium on pair photoproduction and bremsstrahlung, *Phys. Rev. D* 62 (2000) 036008. [doi:10.1103/PhysRevD.62.036008](https://doi.org/10.1103/PhysRevD.62.036008). URL <https://link.aps.org/doi/10.1103/PhysRevD.62.036008>

[19] S. R. Klein, e+ e- pair production from 10-GeV to 10-ZeV, *Radiat. Phys. Chem.* 75 (2006) 696–711. [arXiv:hep-ex/0402028](https://arxiv.org/abs/hep-ex/0402028), [doi:10.1016/j.radphyschem.2005.09.005](https://doi.org/10.1016/j.radphyschem.2005.09.005).

[20] A. B. Migdal, Bremsstrahlung and pair production in condensed media at high-energies, *Phys. Rev.* 103 (1956) 1811–1820. [doi:10.1103/PhysRev.103.1811](https://doi.org/10.1103/PhysRev.103.1811).

[21] L. Gerhardt, S. R. Klein, Electron and Photon Interactions in the Regime of Strong LPM Suppression, *Phys. Rev. D* 82 (2010) 074017. [arXiv:1007.0039](https://arxiv.org/abs/1007.0039), [doi:10.1103/PhysRevD.82.074017](https://doi.org/10.1103/PhysRevD.82.074017).

[22] M. L. Ter-Mikaelian, High energy electromagnetic processes in condensed media, John Wiley & Sons.

[23] P. L. Anthony, et al., Measurement of dielectric suppression of Bremsstrahlung, *Phys. Rev. Lett.* 76 (1996) 3550–3553. [arXiv:hep-ph/9512381](https://arxiv.org/abs/hep-ph/9512381), [doi:10.1103/PhysRevLett.76.3550](https://doi.org/10.1103/PhysRevLett.76.3550).

[24] H. Burkhardt, S. R. Kelner, R. P. Kokoulin, Monte Carlo generator for muon pair production, CERN-SL

97-016-AP.

[astro-ph/9712198](https://arxiv.org/abs/astro-ph/9712198), doi:10.1063/1.56141.

[25] O. Klein, Y. Nishina, Über die Streuung von Strahlung durch freie Elektronen nach der neuen relativistischen Quantendynamik von Dirac, *Zeitschrift fuer Physik* 52 (1929) 853–868. doi:<https://doi.org/10.1007/BF01366453>.

[26] M. Berger, J. Coursey, M. Zucker, J. Chang, Stopping-Power & Range Tables for Electrons, Protons, and Helium Ions, NIST doi:<https://dx.doi.org/10.18434/T4NC7P>.

[27] H. A. Bethe, Zur Theorie des Durchgangs schneller Körpuskularstrahlen durch Materie, *Ann. d. Physik* 397 (1930) 325–400. doi:<https://doi.org/10.1002/andp.19303970303>.

[28] H. A. Bethe, Bremsformel für Elektronen relativistischer Geschwindigkeit, *Z. Phys.* 76 (1932) 293–299. doi:<https://doi.org/10.1007/BF01342532>.

[29] J. Abraham, et al., The Fluorescence Detector of the Pierre Auger Observatory, *Nucl. Instrum. Meth. A* 620 (2010) 227–251. arXiv:0907.4282, doi:10.1016/j.nima.2010.04.023.

[30] H. Tokuno, et al., New air fluorescence detectors employed in the Telescope Array experiment, *Nucl. Instrum. Meth. A* 676 (2012) 54–65. arXiv:1201.0002, doi:10.1016/j.nima.2012.02.044.

[31] B. Rossi, *High Energy Particles*, Prentice-Hall Englewood Cliffs NJ., New Jersey, 1952.

[32] W. R. Nelson, H. Hirayama, D. W. O. Rogers, The Egs4 Code System.

[33] M. Niechciol, M. Risse, P. Ruehl, M. Settimi, P. W. Younk, A. Yushkov, F_γ : A new observable for photon-hadron discrimination in hybrid air shower events, *Astropart. Phys.* 97 (2018) 88–95. arXiv:1710.06586, doi:10.1016/j.astropartphys.2017.10.004.

[34] W. Heitler, *The Quantum Theory of Radiation* Ed. 2, Oxford University Press, London, (1944) p. 234 (Chap 5), 1944.

[35] C. Patrignani, et al., Review of Particle Physics, *Chin. Phys. C* 40 (10) (2016) 100001. doi:10.1088/1674-1137/40/10/100001.

[36] S. R. Klein, Bremsstrahlung and pair creation: Suppression mechanisms and how they affect EHE air showers, *AIP Conf. Proc.* 433 (1) (1998) 132–147. arXiv: